# Control of A Magnetic Actuated Robotic Surgical Camera System for Single Incision Laparoscopic Surgery

Xiaolong Liu[1] and Reza Yazdanpanah A.[1] and Gregory J. Mancini[2] and Jindong Tan[1]

*Abstract*— This paper demonstrates a Magnetic Actuated Robotic Surgical (MARS) camera system with two-degree-of-freedom (2-DOF) orientation control for single incision laparoscopic surgery. The MARS camera design that consists of a stator and a rotor features a unified mechanism for anchoring, navigating, and rotating the insertable camera by externally generated rotational magnetic field from the stator. The insertable camera that has no on-board motors is capsulated in a one-piece housing with two ring-shaped tail-end magnets and one cylindrical central magnet as the rotor. The stator positioned outside an abdominal cavity consists of both permanent magnets and electromagnetic coils to generate rotational magnetic field. A closed-loop control system was developed to enable automatic fine orientation control of the MARS camera. The experimental investigations indicated that our MARS camera can achieve $0.67°$ and $0.49°$ control accuracies for tilt and pan motions respectively.

## I. INTRODUCTION

SINGLE Incision Laparoscopic Surgery (SILS) involves making only one small opening on patient's anatomy to perform surgical procedures. Its benefits include less intra-operative bleeding and post-operative pain, faster recovery, and better cosmetic results compared with multiple-port minimally invasive surgery [1], [2], [3]. But the shared single incision significantly increases the difficulty to manipulate surgical instruments, especially a conventional long stick laparoscopic camera for providing visual feedback.

Insertable cameras with magnetic fixation and positioning for laparoscopic procedures have been reported in [4], [5], [6], [7]. In these solutions, the purpose of the on-board magnetic elements are intended for fixation. Manipulation of the devices for positioning and orientation adjustments is normally achieved by manually maneuvering an external permanent magnet. Researches have focused on developing actuation mechanisms to achieve flexible and automatic control of an inertable laparoscopic camera.

One major challenge to design such actuation mechanisms includes: (1) fixation for holding a camera against an abdominal wall tissue; (2) translation for repositioning a camera at desired location inside an abdominal cavity; and (3) rotation for actuating a camera to its desired orientations. Tethered multiple-link robotic laparoscopic cameras were proposed in [8], which adopt on-board motors and peripheral mechanisms to actuate pan/tilt motion with camera bodies sutured against

[1]Xiaolong Liu, Reza Yazdanpanah Abdolmalaki, and Jindong Tan are with Department of Mechanical, Aerospace and Biomedical Engineering, University of Tennessee, Knoxville, TN 37996, USA {xliu57, ryazdanp}@vols.utk.edu,tan@utk.edu
[2]Gregory J. Mancini is with Department of Surgery, University of Tennessee, Knoxville, TN 37996, USA GMancini@mc.utmck.edu
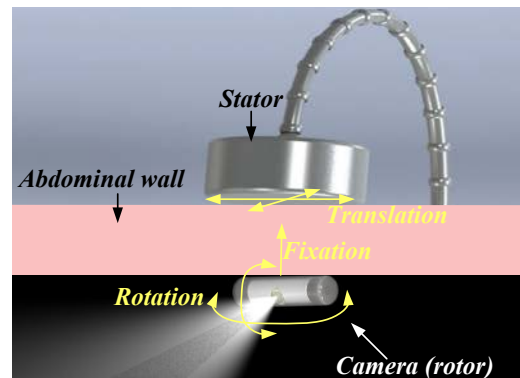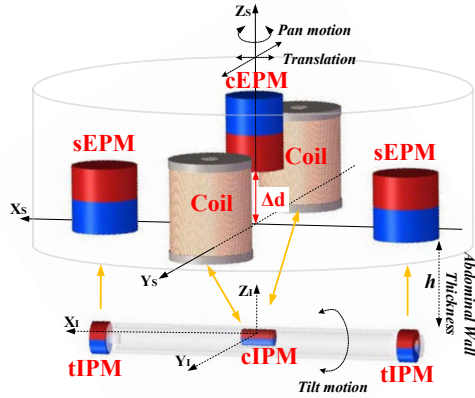
Fig. 1. Conceptual illustration of the MARS camera system.

an abdominal wall for fixation. The laparoscopic camera design in [9] applied a wirelessly controlled motor-driven mechanism for the camera orientation control with an on-board needle pierced through an abdominal wall for the camera fixation and electronics powering. A board-view camera system with a needle for fixation was developed in [10] for providing a wider operating field of view. However, the suturing and needle piercing mechanisms for fixation make the cameras difficult to be repositioned.

To improve the translational function in addition to anchoring for a robotic laparoscopic camera, a magnetic handle provide magnetic coupling with the internal permanent magnets were applied with two on-board motors for both pan and tilt motion control [11]. The designs in [12], [13], [14] replaced pan motion motors by using magnetic coupling between the external handles and on-board permanent magnets to achieve manually actuated pan motion. However, one on-board motor still has to be reserved for tilt motion control in these designs.

Researches so far have addressed separate mechanisms with on-board motors for anchoring, translating, and rotating robotic insertable laparoscopic cameras. However, the on-board motors require not only complex peripheral mechanisms that result in bulky articulated designs, but also consume extra on-board power which leads to short battery life for a wireless camera design. There is a need to develop a unified, motor-free, automatic actuation mechanism for a wireless insertable laparoscopic camera.

In this paper, we propose an orientation control system with less than $1°$ control accuracy for the innovative Magnetic Actuated Robotic Surgical (MARS) camera system developed based on our prior work [15], [16], [17], as conceptually illustrated in Fig. 1. The MARS camera system

Fig. 2. Working principle of the MARS camera system.



Fig. 3. Orientation control architecture of the MARS camera system.

design features a unified, motor-free actuation mechanism for anchoring, navigating, and rotating the camera by externally generated rotational magnetic field. The key component and novelty of the actuation mechanism design is the permanent magnetic driving unit, which is referred to as a rotor, driven externally by a specially designed magnetic stator.

The contributions of this paper beyond our prior work include: 1) an abdominal wall thickness sensing system and a coil current control system were developed for generating appropriate rotational magnetic field to control tilt motion of the MARS camera; 2) a novel stator mechanism was designed to enable automatic pan motion control of the MARS camera; and 3) a fabricated dummy MARS camera system was demonstrated, and experimental analysis was conducted for evaluating the control accuracy of the MARS camera system.

## II. PROBLEM DESCRIPTION OF CAMERA ORIENTATION CONTROL

The magnetic actuation mechanism of the MARS camera illustrated in Fig. 2 consists of (i) a rotor with two tail-end Internal Permanent Magnets (tIPMs) and one central IPM (cIPM), and (ii) a stator with two coils, two side External Permanent Magnets (sEPMs), and one central EPM (cEPM). The stator is positioned externally against an abdominal wall with the EPMs and the coils orthogonally arranged. The rotor is pushed against an abdominal wall internally. The camera body can rotate freely related to the ring-shaped tIPMs which have fixed orientations aligned with the sEPMs. The diametrically magnetized cylindrical cIPM is fixed inside the camera body.

The stator-rotor mechanism is designed to enable orientation, translation, in addition to the compensation of the gravity of the camera (fixation). The camera orientation consists of pan motion and tilt motion. The pan motion requires torque along $Z_I$ axis of the camera, and the tilt motion control requires torque along $X_I$ axis, as shown in Fig. 2. The camera translation requires forces along $X_I, Y_I, Z_I$ axes, with the force along $Z_I$ axis providing the fixation against an abdominal wall. The camera translation control is provided by moving the stator along the dermal surface
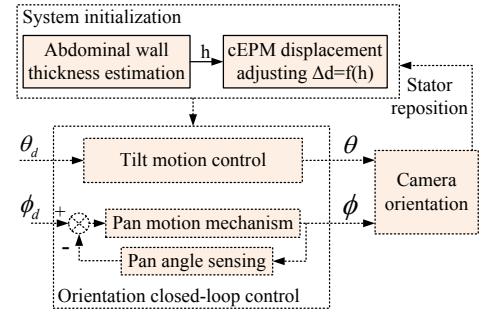
with the attractive forces between the sEPMs and the tIPMs. A spinning motion of the stator along $Z_S$ can actuate the camera's pan motion by the coupled magnetic field of the sEPMs and the tIPMs. Due to the dominant magnetic field from the sEPMs at the location of the cIPM, the camera tilt motion is difficult to be actuated by the activated coils. To eliminate the influence from the sEPMs on the cIPM, the cEPM is applied and adjusted along $Z_S$ with a displacement $\Delta d$ according to an abdominal wall thickness.

The research objective of this paper is to enable automatic orientation control of the MARS camera, which consists of tilt motion and pan motion. To control the tilt motion, the cEPM displacement $\Delta d$ is firstly adjusted according to an abdominal wall thickness $h$. The relationship between an optimal cEPM displacement $\Delta d$ and an abdominal wall thickness $h$ has been formulated as a function $\Delta d = f(h)$ in our prior work [15]. Therefore, the ***first research task*** is to develop an abdominal wall thickness sensing method for estimating $h$, and an automatic cEPM adjusting mechanism for positioning $\Delta d$ based on $\Delta d = f(h)$. With the optimally adjusted cEPM, our ***second research task*** is to develop a closed-loop tilt motion control scheme by controlling the coil current inputs of the stator. To control the camera pan motion, the stator is rotated externally to generate rotational magnetic coupling with the tIPMs in the camera. This function was achieved manually in our prior work [15]. In this paper, the ***third research task*** is to design an automatic pan motion mechanism in the stator for the MARS camera.

## III. CONTROL METHOD OF MAGNETIC ACTUATION MECHANISM

Fig. 3 illustrates the orientation control architecture of the MARS camera. The system initialization is firstly executed by estimating an abdominal wall thickness $h$ and adjusting the displacement $\Delta d$ of the cEPM according to $h$. The input parameters of the control system are the desired tilt angles $\theta_d$ and pan angles $\phi_d$. For tilt motion, the output angle $\theta$ is controlled by the coil current inputs $I_{c1}$ and $I_{c2}$. The pan motion output angle $\phi$ is controlled by an actuation mechanism design presented in Section III-D with a pan motion feedback system.

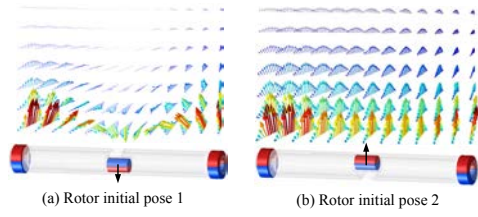(a) Rotor initial pose 1      (b) Rotor initial pose 2

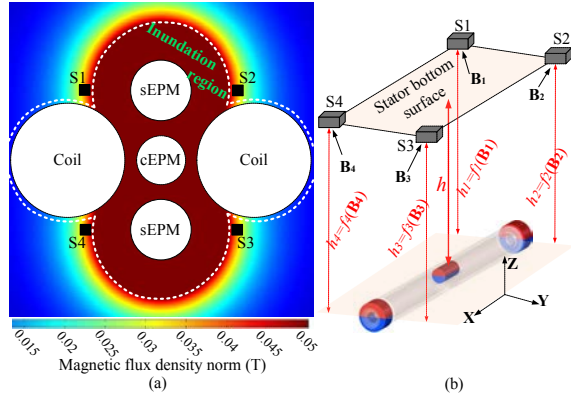Fig. 4. Candidate rotor poses for pre-built magnetic field map.



Fig. 5. Abdominal wall thickness sensing system. (a) Magnetic field sensor configuration at the bottom surface of the stator. (b) Development of magnetic field functions to estimate an abdominal wall thickness $h$.



Fig. 6. cEPM adjusting mechanism in the stator

*A. Abdominal Wall Thickness Estimation*

Benefiting from the fact that the rotor creates a static magnetic field when it's unactuated, the magnetic field of the rotor measured at the stator side varies only according to an abdominal wall thickness $h$. The main idea of estimating $h$ is to sense the rotor magnetic field by using a pre-built rotor magnetic field map which is with respect to different $h$. There are three problems to address for estimating an abdominal wall thickness: 1) the rotor orientation which is used for building the magnetic field map; 2) the configuration of the magnetic field sensors in the stator; and 3) the abdominal wall thickness estimation method with sensed data.

*1) Rotor pose:* The rotor pose determines magnetic field distribution. Fig. 4 shows two desired rotor poses that can generate symmetric magnetic field maps. The rotor poses in Fig. 4(a) and Fig. 4(b) can be actuated by deactivating the coils and adjusting $\Delta d$ of the cEPM to its minimum and maximum respectively. The arrows in Fig. 4 (a) and (b) illustrate the magnetic field strength (proportional to the arrow lengths) and magnetic field direction. It is obvious that the rotor pose in Fig. 4(b) can generate more recognizable magnetic field than that in Fig. 4(a). Therefore, the rotor pose in Fig. 4(b) is selected to build the rotor magnetic field map.

*2) Sensor configuration:* To sense the magnetic field from the rotor, four sets of tri-axis hall effect sensors are installed at the bottom the stator. It is important to select appropriate locations for the sensors to prevent being inundated by the magnetic field from the EPMs. Fig. 5(a) shows the magnetic flux density norm distribution, which is generated by COMSOL Multiphysics 5.0, at the bottom surface of the
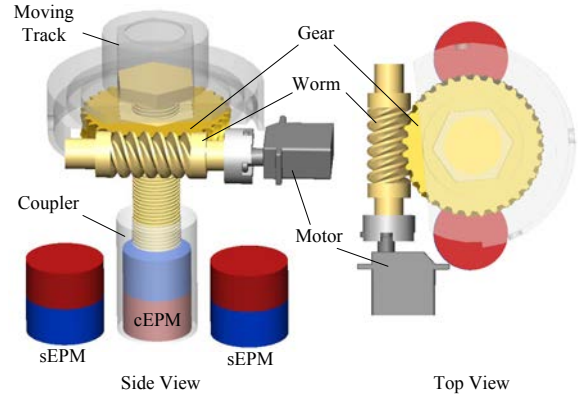
stator. The inundation region in dark red is determined by the measuring ranges of the hall effect sensors. The symmetrically distributed black squares $S_1, S_2, S_3, S_4$ represent the sensor locations which are out of the inundation region and closest to the rotor.

*3) Estimation of h:* Fig. 5(b) shows that the tri-axis hall effect sensors $S_i (i = 1, 2, 3, 4)$ detect magnetic field $\mathbf{B}_i$ from the rotor under an abdominal wall thickness $h$. Due to the magnetic coupling of the EPMs and the IPMs, the positions between the sensors and the rotor are relatively fixed in $X$ and $Y$ directions. A magnetic field map $f_i$ represents the relationship between the rotor magnetic field $\mathbf{B}_i$ as an input and an abdominal wall thickness $h_i$ as an output. The mapping functions $f_i$ represented in lookup tables are developed by recording the magnetic fields $\mathbf{B}_i$ and the adjusted $h_i$.

With the developed $f_i$ and the sensed magnetic fields $\mathbf{B}_i$ by $S_i$, an abdominal wall thickness can be estimated by

$$h = \frac{1}{N} \sum_{i=1}^{N} f_i(\mathbf{B}_i), \tag{1}$$

where $N = 4$ represents the total group number of the hall effect sensors.

*B. cEPM Adjusting Mechanism*

According to the sensed $h$ from Section III-A, the optimal displacements of the cEPM $\Delta d = f(h)$ needs to be adjusted. To enable automatic control, an adjusting mechanism for the cEPM is developed in the stator. Considering the strong magnetic coupling between the cEPM and the sEPMs, the design should be able to provide sufficient actuation force for the cEPM, and also keep a compact stator design.

Fig. 6 shows the conceptual design which is a miniatured motor driven screw jack. The reason to apply such a mechanism is twofold: 1) the lifting force for the cEPM can be efficiently provided by the motor torque through the worm and gear mechanism; 2) the self-locking function of the design enables the cEPM to keep still when the motor is unactuated. The moving track restricts the bolt's rotation, and keeps the bolt and the cEPM moving vertically.
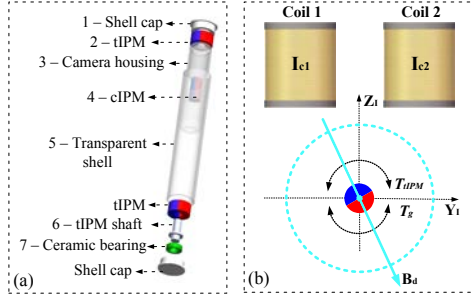
Fig. 7. (a) Conceptual illustration of the rotor design. (b) Rotor tilt motion control with the coils and the cIPM.



Fig. 8. Automatic pan motion mechanism of the stator.

## C. Tilt Motion Control

*1) Camera protection shell:* According to our original rotor design in [15], the camera lens can easily get blurred by peritoneal fluid due to the direct contact with an abdominal wall. To address this issue, a transparent shell, as illustrated in Fig. 7(a)-5, is applied to prevent the camera lens from contacting with tissue and also to maintain imaging quality. Two ceramic bearings (Fig. 7(a)-7) and two tIPM shafts, which are fixed in the shell caps (Fig. 7(a)-1), are used for hanging the camera housing (Fig. 7(a)-3) inside the transparent shell. This design features smooth rotation of the camera housing inside the shell when magnetic torque is exerted on the cIPM (Fig. 7(a)-4). Another benefit of this design is to make the laparoscopic camera reusable by depositing the shell after use, and subsequently reduces a surgery cost.

*2) Control with electromagnetic coils:* The camera tilt motion is activated by the magnetic coupling between the coils and the cIPM. $I_{c1}$ and $I_{c2}$ represent the current inputs of the coils, and $\theta$ represents the camera tilt angle.

The camera protection shell enables the camera free of frictional torque from an abdominal wall during tilt motion. The optimally adjusted cEPM makes the EPMs in the stator generate ignorable impact on the camera tilt motion. Besides the magnetic torque from the coils, the camera tilt motion is also affected by $T_g$ and $T_{tIPM}$ which are the camera gravitational torque along $X_I$ and the magnetic torque from the tIPMs along $X_I$ respectively. Fig. 7(b) shows that $T_g$ and $T_{tIPM}$ are always in opposite directions, which are canceled by each other according to our preliminary experimental investigation. Therefore, the camera tilt angle aligns with the magnetic field direction from the coils. The objective to control the camera tilt motion is to determine $I_{c1}$ and $I_{c2}$ for generating magnetic field with a desired direction $\theta_d$ at the location of the cIPM.

The relationship between $I_{c1}, I_{c2}$ and $\theta_d$ can be formulated by (2) in the stator frame $\Sigma_S$ as follows:

$$\mathbf{B}_{c1}^S I_{c1} + \mathbf{B}_{c2}^S I_{c2} = \underbrace{\mathbf{R}_I^S \mathbf{R}_{Ix}(\theta_d) \mathbf{B}^{-z}}_{\mathbf{B}_d}, \qquad (2)$$

where $\mathbf{R}_I^S \in \mathbb{R}^{3\times3}$ represents a rotation matrix from the rotor internal frame $\Sigma_I$ to the stator frame $\Sigma_S$, as illustrated in Fig. 2. $\mathbf{R}_{Ix}(\theta_d) \in \mathbb{R}^{3\times3}$ represents the rotation matrix along
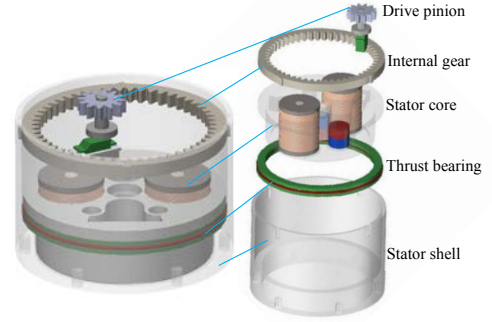
$X_I$. $\mathbf{B}^{-z} \in \mathbb{R}^{3\times1}$ denotes a unit vector pointing in $-Z_I$. $\mathbf{B}_{c1}^S, \mathbf{B}_{c2}^S \in \mathbb{R}^{3\times1}$ denote the unit current magnetic field of the coils at the location of the cIPM. $\mathbf{B}_d \in \mathbb{R}^{3\times1}$ denotes the desired magnetic field direction as shown in Fig. 7(b). Based on the magnetic field models developed in [15], $\mathbf{B}_{c1}^S$, $\mathbf{B}_{c2}^S$ can be computed in real time.

Considering the x components in $\mathbf{B}_{c1}^S$, $\mathbf{B}_{c2}^S$, and $\mathbf{B}_d$ are zeros, (2) is reformulated as

$$\mathbf{B}_d^{yz} = \mathbf{B}_c^{S_{yz}} \mathbf{I}_c, \qquad (3)$$

where $\mathbf{B}_c^{S_{yz}} = [\mathbf{B}_{c1}^{S_{yz}}, \mathbf{B}_{c2}^{S_{yz}}] \in \mathbb{R}^{2\times2}$, $\mathbf{B}_d^{yz} \in \mathbb{R}^{2\times2}$, $\mathbf{I}_c = [I_{c1}, I_{c2}]^T \in \mathbb{R}^{2\times1}$. Because $\mathbf{B}_c^{S_{yz}}$ has a full row rank, the current input vector $\mathbf{I}_c$ can be found in (4) by applying pseudoinverse to (3)

$$\mathbf{I}_c = (\mathbf{B}_c^{S_{yz}})^T (\mathbf{B}_c^{S_{yz}} (\mathbf{B}_c^{S_{yz}})^T)^{-1} \mathbf{B}_d^{yz}. \qquad (4)$$

## D. Pan Motion Mechanism

The camera pan motion is actuated by the stator rotation along $Z_S$ axis due to the magnetic coupling between the EPMs and the tIPMs. To control the pan motion automatically, it is desired to design an actuation mechanism that can generate rotational motion of the stator.

Fig. 8 shows the design of the pan motion mechanism for the stator. The design objective is to control the stator core to rotate inside the stator shell. The motor driven pinion is fixed on the stator core, while an internal gear is attached on the stator shell. The stator core can thus be actuated by the drive pinion and the internal gear. To keep smooth relative rotation between the stator core and the stator shell, a thrust bearing is applied at their contact surfaces.

## IV. PROTOTYPE DEVELOPMENT AND EXPERIMENTAL INVESTIGATION

### A. Experimental Platform

Fig. 9(a) shows the overview of the experimental platform. The camera system was fabricated by a 3D prototyping machine (Fortus 400mc, Stratasys Inc.). To simulate the viscoelastic properties of a real insufflated abdominal wall (average Young's modulus 32.5 kPa) [18], a viscoelastic material Durometer 40 (Young's modulus 27.57 kPa at 15% deflection, Sorbothane, Inc.) was applied. The initial abdominal wall thickness was 26 mm (tissue layer 15 mm, support
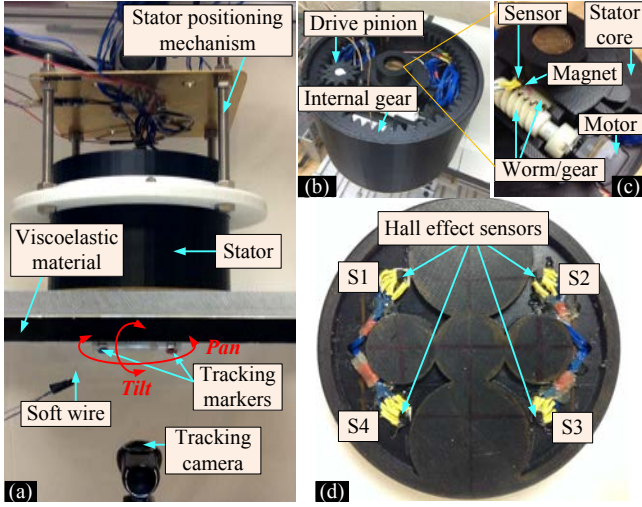
Fig. 9. Experimental platform. (a) System overview. (b) Pan motion mechanism. (c) cEPM adjusting mechanism. (d) Abdominal wall thickness sensing system.
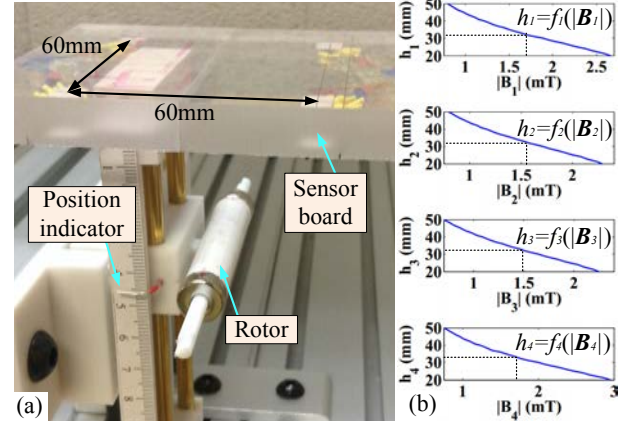


Fig. 10. (a) Experimental setup for building magnetic field map of the rotor. (b) The developed magnetic field maps for estimating an abdominal wall thickness.

layer 11 mm). To increase the abdominal wall thickness for experimental studies, a vertical stator positioning mechanism was developed. A silicone oil lubricated rotor-tissue contact layer was added to the bottom of the viscoelastic material for mimicking an internal abdominal wall surface.

### B. Stator fabrication

*1) cEPM adjusting mechanism:* The fabrication of the cEPM adjusting mechanism proposed in section III-B involves two issues: 1) the mechanism has to provide sufficient lifting force to overcome the magnetic force between the cEPM and the sEPMs; 2) the cEPM has to be accurately controlled to a desired $\Delta d$.

To address the first issue, the required motor torque $M_T$ can be estimated by

$$M_T = \frac{F \cdot p}{2\pi \cdot \eta_s \cdot \eta_{wg} \cdot r},\qquad(5)$$

where $\eta_s$ and $\eta_{wg}$ are the efficiencies of the screw and the worm-gear respectively; $r = 32/3$ is the gear ratio of the worm and gear. According to our experiment, the maximum force used to pull out the cEPM from the magnetic coupling between the cEPM and the sEPMs is about $F = 50$ N. $M_T$ is estimated as 0.149 Nm by conservatively assuming $\eta_s = 10\%$ and $\eta_{wg} = 10\%$. A servo motor (S3156, Futaba Inc.) in Fig. 9(c), which can provide 0.196 Nm at 4.8 V, was modified into continuous rotation for our application.

The second issue can be addressed by applying a magnetic encoder, which is designed by using four tiny cylindrical permanent magnets symmetrically distributed on the gear surface. A single hall effect sensor (CYL8405, Chenyang-Technologies GmbH, Germany) is applied to pickup the magnetic field signal from the magnets to measure the gear rotation. The screw vertically travels 2 mm when the gear generates a full rotation. Four magnets can thus provide the cEPM with 0.5 mm traveling resolution.

*2) Abdominal wall thickness sensing system:* According to the design in Section III-A, the magnetic field sensing system was implemented at the bottom of the stator core, as illustrated in Fig. 9(d). Four sets of tri-axis hall effect sensors (CYL8405, Chenyang-Technologies GmbH, Germany) with measuring ranges 0 ~ 64 mT and sensitivities about 50 mV/mT were symmetrically fixed in the stator core bottom. To enable the sensing system to recognize tiny changes of the rotor magnetic field due to different abdominal wall thicknesses, the measured analog signals were converted to digital signals with the sensing resolution of 0.01 mT by using four 16-bit ADCs (ADS1115, Texas Instruments Inc.).

The estimation function of an abdominal wall thickness developed in (1) was implemented by the data acquired from the experiential setup in Fig. 10(a). The configuration of the hall effect sensors in Fig. 10(a) is the same as that in Fig. 9(d). The rotor with the pose in Fig. 4(b) was fixed on a vertical positioning stage with a distance indicator. Fig. 10(b) shows the mapping functions $f_i, (i = 1, 2, 3, 4)$, which record the norms of the magnetic flux densities $|\mathbf{B}_i|$ and the vertical distances $h_i$ between the rotor and the sensors $S_i$.

*3) Stator core:* According to the design in [15], the stator core consists of two coils, two identical sEPMs and one cEPM. The design specifications are shown in Table I.

*4) Pan motion mechanism:* The fabricated pan motion mechanism is demonstrated in Fig. 9(b). The internal gear has 52 teeth with a pitch diameter 132 mm. The drive pinion has 12 teeth with a pitch diameter 30.48 mm. The stator shell is with an external diameter 164 mm and a height 109 mm. A modified digital servo motor, which is identical to the motor applied to the cEPM adjusting mechanism, is fixed on the stator core and connected with the drive pinion.

*5) Coil current control system:* A tethered current control system was developed, which consists of a micro-controller (STM32F4Discovery, STMicroelectronics Inc.) to generate PWM signals, two PWM amplifiers (L6205 DMOS Full Bridge Driver, STMicroelectronics Inc.) to amplify the signals, a power supply for powering up the amplifiers, and a PC

1400

TABLE I

SPECIFICATIONS OF STATOR CORE AND ROTOR DESIGN

| | |
|---|---|
| Electromagnetic coils: | |
| Dimensions | Height 50 mm, OD 50 mm, ID 10 mm |
| Axial distance | 80 mm |
| Turns | 2,000 |
| Iron-core permeability | 100,000 |
| sEPMs: | Axially magnetized |
| Size | Diameter 25.4 mm, Height 25.4 mm |
| Material | NdFeB Grade N52 |
| Axial distance | 60 mm |
| cEPM: | Axially magnetized |
| Size | Diameter 22.22 mm, Height 28.57 mm |
| Material | NdFeB Grade N52 |
| Camera total length | 79 mm |
| Transparent shell | OD 14.52 mm, ID 13.92 mm |
| Camera housing | OD 12.7 mm, ID 10 mm |
| cIPM: | Diametrically magnetized |
| Size | Diameter 6.35 mm, Length 12.7 mm |
| Material | NdFeB Grade N42 |
| tIPM: | Diametrically magnetized |
| Size | OD 12.7 mm, ID 4.75 mm |
| | Thickness 6.35 mm |
| Material | NdFeB Grade N42 |
| Dummy camera weight | 21.38 g |



Fig. 12. (a) Experiment setup for testing the abdominal wall thickness sensing system. (b) Experiment results that indicate the errors of the sensed distances.
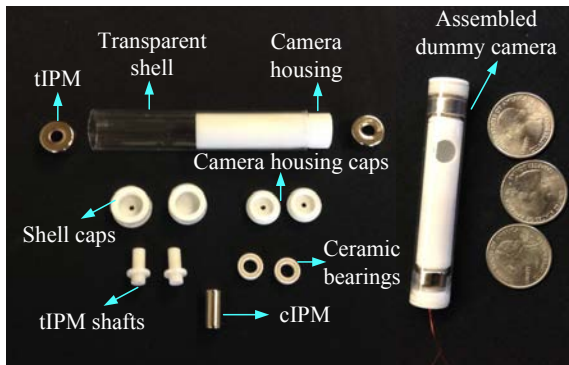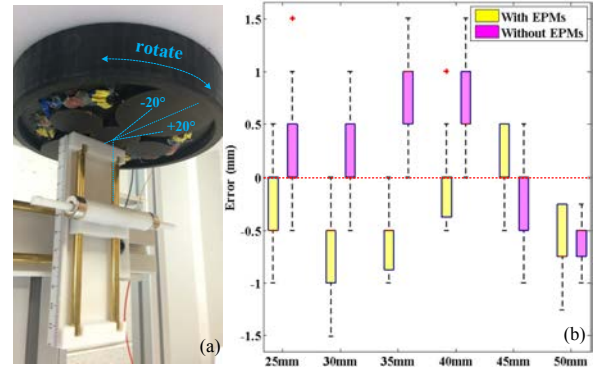


Fig. 11. The disassembled parts and the assembled dummy camera.

computer to send control command to the micro-controller via a serial communication.

### C. Rotor fabrication

Fig. 11 shows the fabricated dummy camera with the disassembled parts. The specifications of the camera is shown in Table I. The outer diameter of the transparent shell (MOCAP, Inc.) determines the camera diameter as 14.52 mm which can fit in a standard trocar with diameter 12 mm ∼ 15 mm. The miniature ceramic ball bearings (NationSkander California Corp.), which have 5 mm inner diameter and 9 mm outer diameter with 3 mm thickness, enable smooth rotation of the camera housing inside the transparent shell.

### D. Evaluation of abdominal wall thickness sensing system

Fig. 12 shows the experimental evaluation for the abdominal wall thickness sensing system developed in Section III-A. To evaluate the sensing accuracy, the experiment was divided into two groups, which were 1) sensing under the impact of the EPMs by using the experimental setup in Fig. 12(a); and 2) sensing without the impact of the EPMs by using the

experimental setup in Fig. 10(a) which were used for building a magnetic field map. To test the reliability and robustness of the sensing system, the stator core in Fig. 12(a) and the sensor board in Fig. 10(a) were rotated within the range of ±20° during each sensing process. Fig. 12(b) shows the errors in detecting the air gaps from 25 mm to 50 mm. The results show that the distance sensing system can provide less than 1 mm accuracy in average for both experiment groups.

### E. Camera Orientation Control

The closed-loop control of the camera orientation requires sensing systems for feedback. Due to the lack of on-board internal sensors at this stage, separate motion feedback systems were designed for pan and tilt motion. The tilt motion sensing system applied a tri-axis accelerometer (LIS331HH, STMicroelectronics Inc.) inside the camera housing with soft wires for power supply and data transmission, as shown in Fig. 9(a). The pan motion sensing system applied a webcam (Logitech Pro 9000) to track the positions of two color markers on the dummy camera. The simulated abdominal wall thickness was adjusted to 35 mm which is about the average value of an normal abdominal wall thickness [18]. The current inputs of the two coils are limited at 1.5 A to prevent coil overheating.

*1) Control of tilt motion:* Fig. 13 shows the tilt motion control experiment by setting the desired tilt angles (red arrows) from 75° to −75° with 15° intervals. The green arrows shows the controlled tilt angles by using the control model developed in Section III-C. Fig. 14 shows the tilt motion control trajectories for the desired tilt angles 15°, 45°, and 75° which took 0.93 s, 1.74 s, and 1.99 s to reach steady states respectively. The average steady-state error of the controlled tilt angles in Fig. 13 and Fig. 14 was 0.67°.

*2) Control of pan motion:* Fig. 15 shows the pan motion control experiment which set the desired pan angles from 0° to 315° with 45° intervals. The drive pinion demonstrated in Fig. 9(b) was activated to rotate the stator core clockwise or counterclockwise accordingly to generate pan motion of the rotor, while the pan motion sensing sytem was detecting the current pan angle for feedback. The red and green arrows
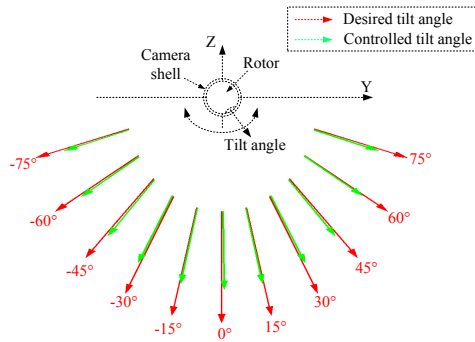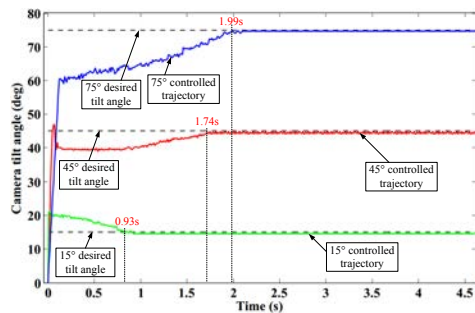
Fig. 13. Tilt motion control experiment.



Fig. 14. Tilt motion control trajectories.



Fig. 15. Pan motion control experiment.

represent the desired pan angles and controlled pan angles respectively. The average control error was 0.49°.

## V. CONCLUSION AND FUTURE WORK

In this paper, a closed-loop control system for a novel insertable laparoscopic camera, i.e. MARS camera, has been presented to enable automatic fine orientation control. The experimental results indicated that the MARS camera control system can achieve 0.67° and 0.49° control accuracies in tilt and pan motions respectively. In our future work, the MARS camera on-board electronics will be integrated especially an inertial sensor which is used to provide the camera orientation feedback wirelessly. The stator cables will be removed by integrating a wireless module, coil drivers, and batteries inside the stator. The MARS camera system will also be tested *in vivo* by using a porcine abdominal cavity.

## REFERENCES

[1] M. Desai, A. Berger, R. Brandina, M. Aron, B. Irwin, D. Canes, M. Desai, P. Rao, R. Sotelo, R. Stein, and I. Gill, "Laparoendoscopic single-site surgery: Initial hundred patients," *Urology*, vol. 74, no. 4, pp. 805 – 812, 2009.

[2] M. Saidy, M. Tessier, and D. Tessier, "Single-incision laparoscopic surger–hype or reality: A historical control study," *Perm J.*, vol. 16, no. 1, pp. 47–50, 2012.

[3] C. Tracy, J. Raman, J. A. Cadeddu, and A. Rane, "Laparoendoscopic single-site surgery in urology: where have we been and where are we heading?," *Nat Clin Pract Urol.*, vol. 5, no. 10, pp. 561–568, 2008.

[4] M. Fakhry, B. Gallagher, F. Bello, and G. Hanna, "Visual exposure using single-handed magnet-driven intra-abdominal wireless camera in minimal access surgery: is better than 30 degrees endoscope.," *Surg Endosc.*, vol. 23, no. 3, pp. 539–543, 2009.

[5] P. Swain, R. Austin, K. Bally, and R. Trusty, "Development and testing of a tethered, independent camera for notes and single-site laparoscopic procedures.," *Surg Endosc.*, vol. 24, no. 8, pp. 2013–21, 2010.
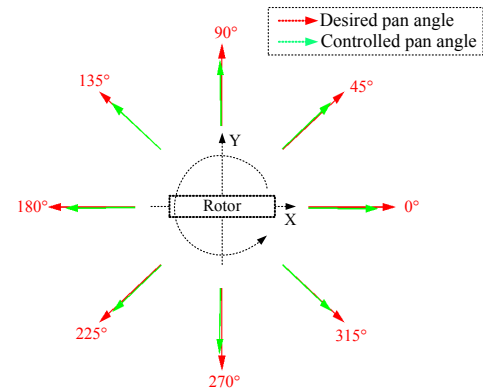
[6] J. Cadeddu, R. Fernandez, M. Desai, R. Bergs, C. Tracy, S. Tang, P. Rao, M. Desai, and D. Scott, "Novel magnetically guided intra-abdominal camera to facilitate laparoendoscopic single-site surgery: initial human experience.," *Surg Endosc.*, vol. 23, no. 8, pp. 1894–9, 2009.

[7] M. Silvestri, T. Ranzani, A. Argiolas, M. Vatteroni, and A. Menciassi, "A multi-point of view 3d camera system for minimally invasive surgery," *Sensors and Actuators A: Physical*, vol. 202, pp. 204 – 210, 2013.

[8] T. Hu, K. Allen, J. Hogle, and L. Fowler, "Insertable surgical imaging device with pan, tilt, zoom, and lighting," *The International Journal of Robotics Research*, vol. 28, no. 10, pp. 1373–1386, 2009.

[9] C. Castro, S. Smith, A. Alqassis, T. ketterl, S. Yu, S. Ross, A. Rosemurgy, P. Savage, and R. Gitlin, "A wireless robot for networked laparoscopy," *Biomedical Engineering, IEEE Transactions on*, vol. 60, no. 4, pp. 930–936, 2013.

[10] T. Kawahara, T. Takaki, I. Ishii, and M. Okajima, "Development of a broad-view camera system for minimally invasive surgery," in *Intelligent Robots and Systems (IROS), 2010 IEEE/RSJ International Conference on*, pp. 2810–2815, Oct 2010.

[11] B. Terry, Z. Mills, J. Schoen, and M. Rentschler, "Single-port-access surgery with a novel magnet camera system," *Biomedical Engineering, IEEE Transactions on*, vol. 59, pp. 1187–1193, April 2012.

[12] S. Platt, J. Hawks, and M. Rentschler, "Vision and task assistance using modular wireless in vivo surgical robots," *Biomedical Engineering, IEEE Transactions on*, vol. 56, no. 6, pp. 1700 –1710, 2009.

[13] M. Simi, M. Silvestri, C. Cavallotti, M. Vatteroni, P. Valdastri, A. Menciassi, and P. Dario, "Magnetically activated stereoscopic vision system for laparoendoscopic single-site surgery," *Mechatronics, IEEE/ASME Transactions on*, vol. 18, no. 3, pp. 1140–1151, 2013.

[14] M. Simi, G. Sardi, P. Valdastri, A. Menciassi, and P. Dario, "Magnetic levitation camera robot for endoscopic surgery," in *Robotics and Automation (ICRA), 2011 IEEE International Conference on*, pp. 5279–5284, 2011.

[15] X. Liu, G. J. Mancini, and J. Tan, "Design and analysis of a magnetic actuated capsule camera robot for single incision laparoscopic surgery," in *Intelligent Robots and Systems (IROS), 2015 IEEE/RSJ International Conference on*, 2015.

[16] X. Liu, G. Mancini, and J. Tan, "Design of a unified active locomotion mechanism for a capsule-shaped laparoscopic camera system," in *Robotics and Automation (ICRA), 2014 IEEE International Conference on*, pp. 2449–2456, 2014.

[17] X. Liu, G. J. Mancini, and J. Tan, "Design of a unified active locomotion mechanism for a wireless laparoscopic camera system," in *Intelligent Robots and Systems (IROS), 2014 IEEE/RSJ International Conference on*, pp. 1294–1301, 2014.

[18] C. Song, A. Alijani, T. Frank, G. Hanna, and A. Cuschieri, "Mechanical properties of the human abdominal wall measured in vivo during insufflation for laparoscopic surgery," *Surgical Endoscopy And Other Interventional Techniques*, vol. 20, no. 6, pp. 987–990, 2006.